



## Robust spatial fuzzy GMM based MRI segmentation and carotid artery plaque detection in ultrasound images

Mehdi Hassan<sup>a,\*</sup>, Iqbal Murtza<sup>a</sup>, Aysha Hira<sup>a</sup>, Safdar Ali<sup>b</sup>, Kashif Kifayat<sup>a</sup>

<sup>a</sup> Department of Computer Science, Air University Sector E-9, PAF Complex, Islamabad, Pakistan

<sup>b</sup> Directorate General National Repository, Islamabad, Pakistan



### ARTICLE INFO

#### Article history:

Received 1 February 2019

Revised 27 March 2019

Accepted 22 April 2019

#### Keywords:

Soft clustering  
Expectation maximization  
Carotid Plaque  
SVM  
GMM

### ABSTRACT

**Background and Objective:** In medical image analysis for disease diagnosis, segmentation is one of the challenging tasks. Owing to the inherited degradations in MRI improper segments are produced. Segmentation process is an important step in brain tissue analysis. Moreover, an early detection of plaque in carotid artery using ultrasound images may prevent serious brain strokes. Unfortunately, low quality and noisy ultrasound images are still challenges for accurate segmentation. The objective of this research is to develop a robust segmentation approach for medical images such as brain MRI and carotid artery ultrasound images.

**Methods:** In this paper, a novel approach is proposed to address the segmentation challenges of medical images. The proposed approach employed fuzzy intelligence and Gaussian mixture model (GMM). It comprises two phases; firstly, incorporating spatial fuzzy c-means in GMM by exploiting statistical, texture, and wavelet image features. During model development, GMM parameters are estimated in presence of noise by EM algorithm iteratively. Utilizing these parameters, brain MRI images are segmented. In next phase, developed approach is applied to solve a real problem of carotid artery plaque detection using ultrasound images. The dataset of real patients annotated by radiologists has been obtained from Radiology Department, Shifa International Hospital Islamabad, Pakistan. For this, intima-media-thickness values are computed from the proposed segmentation followed by support vector machines for plaque classification (normal/abnormal).

**Results:** The obtained segmentation has been evaluated on standard brain MRI dataset and offers high segmentation accuracy of 99.2%. The proposed approach outperforms in term of segmentation performance range of 3–9% as compared to the state of the art approaches on brain MRI. Furthermore, the proposed approach shows robustness to various levels of Gaussian and Rician image noises. On carotid artery dataset, we have obtained high plaque detection rate in terms of accuracy, sensitivity, specificity, and F-score values of 98.8%, 99.3%, 98.0%, and 97.5% respectively.

**Conclusions:** The proposed approach segments both modalities with high precision and shows robustness at Gaussian and Rician noise levels. Results for brain MRI and ultrasound images indicate its effectiveness and can be used as second opinion in addition to the radiologists. The developed approach is straightforward, efficient, and reproducible. It may benefit to improve the clinical evaluation of the disease in both asymptomatic and symptomatic individuals.

© 2019 Elsevier B.V. All rights reserved.

### 1. Introduction

In medical image processing and disease diagnosis, segmentation is one of the challenging tasks. Segmentation helps precise identification of objects presented in an image by segregating image contents into non-overlapping regions based on pixel intensity, spatial information, or/and image features [1]. It has a

significant role in various medical image analysis tasks such as tissue volume quantification [2], rehabilitation [3], anatomical studies [4], diagnosis [5–7], and computer-assisted surgery [8].

Among the neurologists, magnetic resonance imaging (MRI) is a popular imaging modality which is helpful for examining and analysis up to tissue level. Moreover, MRI is used for observing the brain internal structure for disease diagnosis such as tumor, scalp fractures, and internal bleedings. Unfortunately, brain MRI may have inherent superfluous intensity variations during acquisition process. Furthermore, the presence of bias field known as intensity non-uniformity or intensity inhomogeneity is a major barrier

\* Corresponding author.

E-mail address: [mehdi.hassan@mail.au.edu.pk](mailto:mehdi.hassan@mail.au.edu.pk) (M. Hassan).

being faced by neurologists for analyzing brain MRI. Owing to intensity inhomogeneity the expert opinions for analyzing these images may vary consequently risking inaccurate diagnosis [9].

Cerebrovascular disease is the fourth leading cause of deaths in United States for year 2010 [10]. There are two categories of cerebrovascular attacks namely, *Ischemic* and the *Hemorrhagic* strokes. These strokes occur because of carotid artery plaque and raptures of brain blood vessel, respectively. Early blockage detection may reduce the risk of such strokes.

Carotid angiography (uses X-ray imaging) is considered as a standard technique for the plaque detection in carotid artery caused by fatty materials. Owing to these plaques, the flow of oxygenated blood to brain may be partially or fully blocked and consequently, risking a brain stroke. Additionally, if plaque ruptures, its particles may drift into the brain and causing cerebrovascular attack. These risks create the demand of early and accurate detection of carotid plaque to prevent such serious effects. Unfortunately, angiography has some drawbacks such as patient distress, allergic reactions, radiation hazards, and kidney failure because of invasive nature (an injection of material into the blood vessels).

In contrast, the medical imaging modalities such as MRI, computed tomography (CT), and ultrasound allows acquiring subject's scan non-invasively. The diagnosis process based on these modalities requires substantial effort of medical expert from massive streams of images. To reduce this effort, an appropriate computer aided diagnosis (CAD) is highly demanded to assist radiologists for analysis and disease diagnosis. These automated systems firstly perform segmentation followed by post-processing steps on these images. In literature, numerous techniques are available for medical image segmentation [11–14], but most of them coup with either noise or low image quality [15].

Organization of the paper is as follows; [Section 2](#) describes the comprehensive literature review. The proposed methodology is explained in [Section 3](#) whereas; [Section 4](#) presents experimental results and [Section 5](#) includes discussions. Lastly, [Section 6](#) concludes this research and recommends the future directions.

## 2. Related work

In recent years, the development of imaging techniques has played a significant role in healthcare sector. Owing to these advances, radiologists are being assisted by automated and intelligent computational techniques [16]. Among these imaging techniques, MRI has shown a significant role in healthcare as well as neuroscience research for the study of human brain structure. Unluckily, MRI possesses the limitations of intensity inhomogeneity and non-uniform magnetic field which may result improper segmentation for disease diagnosis. Thus to get an appropriate segmented image, intensity non-uniformity in brain MRI needs to be addressed. The following paragraphs describe various segmentation techniques for medical images reported in the literature.

Nguyen and Wu reported a GMM based technique for medical image segmentation [17]. The authors have focused on the incorporation of pixel neighborhood information mapped into the GMM based Markov random field. Unluckily, the successful convergence of their technique critically depends upon precise prior probabilities. Additionally, the presence of noise results in either over or under segmentation.

Mayer and Greenspan proposed a segmentation technique for MRI using mean shift method [18]. In mean shift algorithm, cluster centers are marked based on density to perform clustering. This iterative and user intervention may make the model computationally expensive and user dependent.

Wang et al. [19] reported a robust soft segmentation algorithm which utilizes pixel spatial information for medical images. Their

technique composed of two steps: firstly, the conventional FCM is used for initial clustering labels. Whereas; in the next step, a scanning window is performed on FCM segmented image to reduce mislabel pixels. As the noise level increases, the algorithm offers in-homogenous segments.

Incremental neural network technique used for segmentation of various medical imaging modalities has been presented by Iscan et al. [20]. In their technique, segmentation is performed utilizing multiple image features. Similarly, Benaichouche et al. has proposed a hybrid clustering approach for image segmentation consisting of three levels [21]; (1) particle swarm optimization (PSO) in conjunction with FCM is used for initialization (2) combination of spatial knowledge is used for image segmentation to minimize the geometrical shape effect (3) the segmentation results are enhanced by redistributing the potentially mislabeled pixels. In their approach, the lengthy training process of PSO is computationally expensive.

Ji et al. [22] introduced a fuzzy weighted clustering approach in which anisotropic weights are assigned to each patch. In order to get the weights, mean deviation was applied into exponential kernel function. But, the selection of patch size is very subjective and may affect the segmentation results. In another work, Ji et al. [23] proposed image segmentation approach which utilizes spatially constrained FCM. Their technique uses a regularization factor of probabilistic neighborhood directions. This is followed by different combinations of orthogonal polynomials for estimation of bias field. Then, four pre-defined filters are convolved for each direction to find the probabilities. It is challenging to find the optimal direction and filter size. Additionally, the regularization factor may blur the image yielding under segments.

The effectiveness of the post-processing steps are mainly depends upon segmentation accuracy. A minor variation in image segments may affect these steps, and produces misleading results. Alternatively, a slight enhancement in segmentation may increase the efficacy of disease diagnosis. Thus, an accurate image segmentation technique has substantial influence for the development of CAD systems.

Nevertheless, medical images inherit some basic problems including poor resolution, presence of noise, partial volume effect, and other degradations [24]. Due to these limitations, segmentation of such images is challenging and may produce misdiagnosis. For example, ultrasound images are mostly suffered by poor resolution, speckle noise, and electromagnetic interferences [25].

Chuang et al. [26] have proposed medical image segmentation technique which comprises of spatial information incorporated into basic FCM framework by exploiting pixel's spatial information namely sFCM. However, their approach assigns uniform weightage to all pixels of  $m \times m$  window generating non-homogenous clusters. In this direction, Chaudhry et al. [27] have modified sFCM by assigning a non-uniform weight to each pixel of the window. Likewise, Li et al. [28] have proposed an approach for segmenting medical images by incorporating level-set methods into sFCM framework. By the incorporation of partial differential equations, their approach becomes computationally expensive. Hassan et al. [29] have proposed a segmentation approach for ultrasound image by exploiting ensemble clustering, hybrid features, genetic algorithm, and neural networks. Unfortunately, their approach shows low resilience to high noise levels.

## 3. Material and methods

### 3.1. Datasets

The first dataset has been obtained from the BrainWeb [30] which contains 20 synthetic brain MRI of voxel size  $1.0 \times 1.0 \times 1.0$  having dimension of  $217 \times 181$  and intensity non-

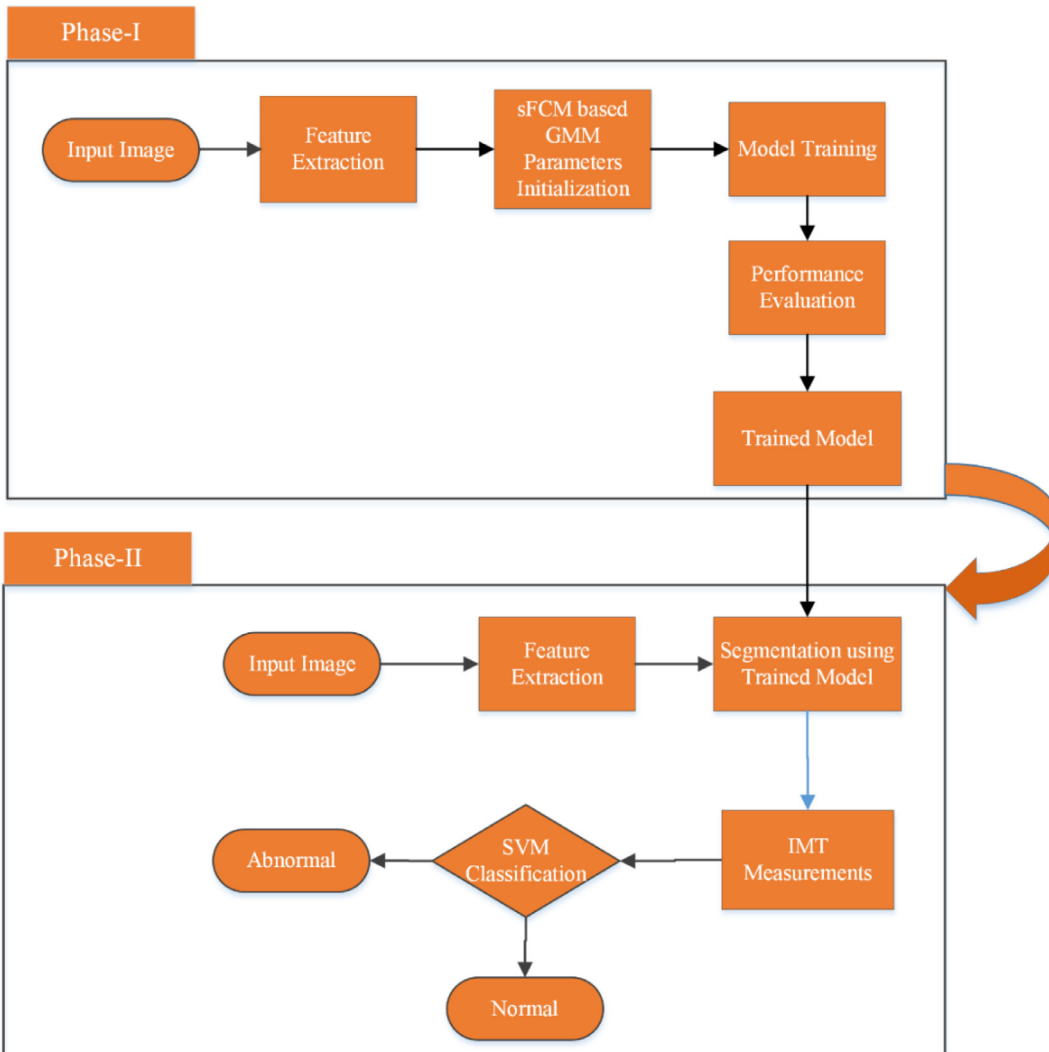


**Fig. 1.** Block diagram of the proposed methodology.

uniformity ranging 0~100%. In this dataset, the ground truths are available for performance comparison.

The second dataset consists of real carotid artery ultrasound images acquired from Shifa International Hospital Ltd., Islamabad, Pakistan containing 45 subjects. The images of this dataset have been extracted from videos using Toshiba's Xario XG with linear probe transducer of frequency ranging 7–8 MHz. This dataset comprises of 250 images annotated by the radiologist of the hospital in which 150 are normal and 100 are abnormal. For annotation, multiple images (3–6) of each subject have been selected hence used in this experiment. Region of interest (ROI) of each frame is marked as normal or abnormal carotid artery by the medical experts for model evaluation. In this dataset, the images have  $800 \times 600$  size with resolution of 72 pixels per inch (PPI). The original image were cropped into the size of  $350 \times 380$ . The subjects involved in this dataset aging 35–74 years with mean and standard deviation of 55.75 and 9.43, respectively.

### 3.2. Methods

The proposed approach comprises of two phases; (1) formation of a segmentation model and (2) application to carotid artery plaque detection. The block diagram of the proposed methodology is shown in Fig. 1 and explained subsequently.

#### 3.2.1. Formation of segmentation model

In this phase, a segmentation model is developed for medical images using multiple features, sFCM, and GMM. The components are explained below:

**3.2.1.1. Feature extraction.** First of all, a feature vector is formulated for each image pixel before it may feed as input for segmentation. These features have an ability to represent the image in better way and also reduce the effect of noise as well. Three types of image descriptors namely, MGH, CWT, and GLCM are extracted which are extensively used in the literature especially for medical images. We have extracted a total of 39 (MGH, CWT, and GLCM) features for every pixel used for segmentation. The detail of each features type is given below:

**Moments of gray level histogram (MGH).** The MGH image descriptors utilize intensity histogram extracted for a sub-image. A total of nine features including smoothness, uniformity, entropy, mean, standard deviation, third, seventh, eighth, and ninth central moments are obtained from input image [11,20,31]. The  $n^{th}$ -order moment around the intensity mean  $m$  (central moment) is computed as below:

$$u_n = \sum_{i=0}^{L-1} (z_i - m)^n \cdot p(z_i) \quad (1)$$

where  $p(z_i)$  is relative frequency of gray level  $z_i$  and  $L$  is the total intensity levels of image.

The following statistical characteristics are extracted from the input image:

$$\text{mean} = \sum_{i=0}^{L-1} z_i p(z_i) \quad (2)$$

$$\sigma = \sqrt{u_2} \quad (3)$$

$$\text{Smoothness} = 1 - \frac{1}{1 + \sigma} \quad (4)$$

$$u_3 = \sum_{i=0}^{L-1} (z_i - m)^3 \cdot p(z_i) \quad (5)$$

$$\text{Uniformity} = \sum_{i=0}^{L-1} p^2(z_i) \quad (6)$$

$$\text{Entropy} = - \sum_{i=0}^{L-1} p(z_i) \cdot \log_2(p(z_i)) \quad (7)$$

$$F7 = \sum_{i=0}^{L-1} p^3(z_i) \quad (8)$$

$$F8 = \sum_{i=0}^{L-1} p^4(z_i) \quad (9)$$

$$F9 = \sum_{i=0}^{L-1} p^5(z_i) \quad (10)$$

The features  $F7-F9$  are included in to enrich statistical characteristic of pixel as reported in the literature [32].

*Continuous wavelet transforms (CWT).* In image analysis 2-D CWT offers robust feature representation. To address the issue of computational time, the cover map concept is introduced [33,34]. The CWT function is given below:

$$\psi_{u,s,\theta}(x) = \frac{1}{s} \psi\left(r_{-\theta}\left(\frac{x-u}{s}\right)\right) \quad (11)$$

where  $u$ ,  $s$ , and  $\theta$  are translation, scaling, and rotation parameters, respectively and the parameter  $r_\theta$  is rotation matrix. In this research, the default values of  $u$  and  $\theta$  are used ( $u=\theta=0$ ), whereas,  $s$  factor is varied for the whole dataset.

2D-CWT is applied to the input images on various scales generating different output images to explore lower and higher frequency bands. The smooth image areas are visible at higher  $s$  values whereas, the edges are visible at lower  $s$  values. Scale parameter values ranging 1–10 are employed to extract features for segmentation. It is empirically found that eight  $s$  values (1.0, 1.6, 2.6, 3.9, 4.0, 5.0, 5.4 and 7.0) are sufficient to yield quality segmentation and the remaining features do not have significant impact [11,20]. In our experiments, we have extracted a total of eight CWT features by utilizing a  $7 \times 7$  window size.

*Gray level co-occurrence matrix (GLCM).* The GLCM comprises of statistical measures which explore pixel spatial relationships. These relationships can find various adjacencies such as horizontal, diagonal, and off-diagonal. The outcome of the relationship is simply a frequency of joint pixel occurrences. In this research, 22 GLCM features are extracted using  $7 \times 7$  window size and detail these features as given below [11,35].

$$\text{Contrast} : \sum_{n=0}^{N_g-1} n^2 \left\{ \sum_{\substack{i=1 \\ |i-j|=n}}^{N_g} \sum_{j=1}^{N_g} p(i, j) \right\},$$

$$\text{Correlation} = \frac{\sum \sum (ij)p(i, j) - \mu_x \mu_y}{\sigma_x \sigma_y},$$

$$\text{Sum of Squares} = \sum_i \sum_j (i - \mu)^2 p(i, j),$$

$$\text{Inverse Difference Moment} = \sum_i \sum_j \frac{1}{1 + (i - j)^2} p(i, j),$$

$$\text{Sum Average} = \sum_{i=2}^{2N_g} i p_{x+y}(i),$$

$$\text{Sum Variance} = \sum_{i=2}^{2N_g} (i - f_8)^2 p_{x+y}(i), \text{ where } f_8 \text{ is sum Entropy}$$

$$\text{Sum Entropy} = - \sum_{i=2}^{2N_g} p_{x+y}(i) \log \{p_{x+y}(i)\},$$

$$\text{Entropy} = - \sum_i \sum_j p(i, j) \log (p(i, j))$$

$$\text{Difference Variance} = \text{variance of } p_{x-y}$$

$$\text{Difference Entropy} = - \sum_{i=0}^{N_g-1} p_{x-y}(i) \log \{p_{x-y}(i)\}$$

$$\text{Information Measure of Correlation (IMC)} :$$

$$\text{IMC1} = \frac{HXY - HXY1}{\max\{HX, HY\}}$$

$$\text{IMC2} = (1 - \exp[-2.0(HXY2 - HXY)])^{1/2}$$

$$HXY = - \sum_i \sum_j p(i, j) \log (p(i, j))$$

$$\text{where } HX \text{ and } HY \text{ are entropies of } p_x \text{ and } p_y, \text{ and } HXY1 = - \sum_i \sum_j p(i, j) \log \{p_x(i) p_y(j)\} \quad HXY2 = - \sum_i \sum_j p_x(i) p_y(j) \log \{p_x(i) p_y(j)\}.$$

$$\text{Homogeneity} = \sum_{i=0}^{N-1} \sum_{j=0}^{N-1} \frac{P_{i,j}}{(i - j)^2},$$

$$\text{Dissimilarity} = \sum_{i=0}^{N-1} \sum_{j=0}^{N-1} P_{i,j} |i - j|,$$

In addition to above features, maximum probability, cluster prominence, cluster shade, and autocorrelation are also obtained from the input image.

**3.2.1.2. Spatial fuzzy c-means.** FCM is a soft clustering technique being successfully employed in the area of pattern recognition. FCM is a strong candidate approach especially when there are overlapping regions. Owing to overlapping nature of human organs, there is possibility that a pixel of medical image may belongs to multiple segments with different membership degree. Thereby, soft clustering is quite helpful in segmenting the complex brain MRI where, most of the regions are overlapped.

The FCM cost function is given as:

$$J_{FCM} = \sum_{i=1}^N \sum_{j=1}^C u_{ij}^m d_{ij} \quad (12)$$

where,  $m \in (1, \infty)$  and  $d_{ij}$  are fuzziness degree and  $L_2$  norm between intensity level  $i$  and  $j^{th}$  cluster center  $C_j$ , respectively. Fuzzy clustering process is carried out iteratively which updates membership values  $u_{ij}$  and cluster centroids  $C_j$  using the Eqs. (13)–(14). The membership values are initialized randomly [36].

$$c_j = \frac{\sum_{i=1}^N u_{ij}^m x_i}{\sum_{i=1}^N u_{ij}^m} \quad (13)$$

$$u_{ij} = \frac{1}{\sum_{k=1}^C \left( \frac{\|x_i - c_k\|}{\|x_i - c_j\|} \right)^{\frac{2}{m-1}}} \quad (14)$$

The FCM does not utilize any spatial information which is susceptible to noise. For robustness, spatial information may be incorporated into conventional FCM. Due to the high correlation of image pixels, it is possible that pixels may be part of multiple segments. Keeping in mind this concept, spatial information of the pixels is explored. Chuang et al. modified the conventional FCM by the incorporation of spatial information [37] in which the following kernel is used to consider spatial information:

$$h_{ij} = \sum_{k \in NB(x_j)} u_{ik} \quad (15)$$

where  $NB(x_j)$  represents neighborhood of pixel  $x$  for cluster  $j$ . In this research, the kernel size of  $5 \times 5$  has been employed. The kernel mentioned in Eq. (15) has been integrated into FCM membership as under:

$$u_{ij} = \frac{u_{ij}^p h_{ij}^q}{\sum_{k=1}^C u_{kj}^p h_{kj}^q} \quad (16)$$

where  $p$  and  $q$  are controlling parameters of sFCM membership function.

For better clustering, we utilize the sFCM technique in conjunction with GMM. In the following sub-sections, we elaborate the utilization of GMM. GMM parameters are estimated by EM algorithm which is an iterative estimation technique and widely used in signal processing. Brain MRI and carotid artery ultrasound images have inherited degradations such as Gaussian, Rician, and Spackle noises, respectively. The EM algorithm is employed to estimate the latent variables in the presence of noise.

**Gaussian mixture model (GMM).** GMM is a probabilistic model and can be used as soft classifier [38]. It is defined as the weighted sum of multiple Gaussians distributions which is utilized for unsupervised image segmentation [23]. The GMM density function is given as below:

$$f(x_i | \prod, \theta) = \sum_{j=1}^L \pi_{ij} P(x_i | \theta_j) \quad (17)$$

where  $\pi_{ij}$ ,  $i=(1, 2, \dots, P)$ ,  $j=(1, 2, \dots, L)$  are prior probabilities (occurring frequencies) of pixel  $x_i$  to belong region  $\theta_j$ . The  $P(x_i | \theta_j)$

is the Gaussian distribution of region  $\theta_j$  where,

$$0 \leq \pi_{ij} \leq 1 \text{ and } \sum_{j=1}^L \pi_{ij} = 1 \quad (18)$$

The components of feature vector  $x_i$ ,  $i=1: n$  are considered as mutually exclusive. Thus, joint conditional probability over the whole image is derived as follows:

$$p(x | \prod, \theta) = \prod_{i=1}^P f(x_i | \prod, \theta) = \prod_{i=1}^P \sum_{j=1}^L \pi_{ij} P(x_i | \theta_j) \quad (19)$$

The maximum likelihood function used in EM is applied for estimation of GMM parameters.

**Expectation maximization (EM) algorithm.** The density function for Gaussian distribution is given as:

$$p(x) = \sum_{k=1}^K \pi_k P(x | \theta_k) \quad (20)$$

where  $P(x_i | \theta_j)$  is the Gaussian distribution with parameters  $\theta = (\mu, \sigma)$

If all the points  $x \in X$  are the mixtures of  $K$  Gaussians, each point  $x_i$  is probabilistically assigned to  $k^{th}$  Gaussian distribution. One can define the probability that the point  $x_i$  is generated by  $k^{th}$  Gaussian as:

$$p(X) = \prod_{i=1}^n p(x_i) = \prod_{i=1}^n \sum_{k=1}^K \pi_k P(x_i | \theta_k) \quad (21)$$

The objective is to find  $\pi_k$  and  $\theta_k$  such that  $p(X)$  is maximized. To estimate maximum likelihood function for  $\theta$ , log-likelihood function is defined as:

$$L(\theta) = \ln p(X | \theta) \quad (22)$$

$\ln(x)$  is a monotonically increasing function. Hence, the optimal parameter  $\theta$  can be determined by the maximization of  $p(X | \theta)$ . EM algorithm is an iterative method maximizing the value of  $L(\theta)$ . To maximize  $L(\theta)$ , the updated estimate for  $\theta$  is computed as [39]:

$$L(\theta) > L(\theta_n) \quad (23)$$

$p(X)$  is maximized as:

$$L(\theta) = \sum_{i=1}^n \ln \left\{ \sum_{k=1}^K \pi_k P(x_i | \theta_k) \right\} \quad (24)$$

For each Gaussian cluster having various number of data points  $x_i$ , total weight  $S_k$  is defined as follows:

$$S_k = \sum_{i=1}^n w_{ik} \quad (25)$$

Weighted mean  $u_k$  and weighted variance  $\sigma_k$  is defined below:

$$u_k = \frac{1}{S_k} \sum_{i=1}^n w_{ik} x_i \quad (26)$$

$$\sigma_k = \frac{1}{S_k} \sum_{i=1}^n w_{ik} (x_i - u_k) x_i (x_i - u_k)^T \quad (27)$$

Based on these equations, EM algorithm proceeds as under:

**Expectation step.** Initialize the means  $u_k$ , variances  $\sigma_k$ . Mixing the coefficients  $\pi_k$  and evaluate the initial log-likelihood function as following,

$$w_{ik} = \frac{\pi_k P(x_i | \theta_k)}{\sum_{j=1}^K \pi_j P(x_i | \theta_k)} \quad (28)$$

*Maximization step.* This step updates parameters by utilizing Eqs. (29) and (30) iteratively to obtain  $\theta_k$ .

$$u_k^{new} = \frac{1}{S_k} \sum_{i=1}^n w_{ik} x_i \quad (29)$$

$$\sigma_k^{new} = \frac{1}{S_k} \sum_{i=1}^n w_{ik} (x_i - u_k^{new}) x_i (x_i - u_k^{new})^T \quad (30)$$

The function given in Eq. (22) iteratively updates the GMM parameters until stopping condition met. The convergence criteria comprised matching of GMM generated cluster labels with sFCM or maximum iterations (in our case we set equal to 500). In next step, cluster labels are predicted using the following expression.

$$\theta_{ik} = \sqrt{\sum_{j=1}^n \left[ \frac{\mathbf{X}_{ij} - u}{\sigma} \right]^2} \text{ for } k = 1, 2, \dots, C \quad (31)$$

where,  $\mathbf{X}_{ij}$  is the  $j^{th}$  component of the  $i^{th}$  input data element and  $k$  is the number of clusters. Whereas,  $u$  and  $\sigma$  are mean and standard deviation, respectively. The parameter  $\theta$  is computed once for each image modality and thus, used to segment the input images [40]. The output fuzzy cluster labels are computed by the following expression:

$$y_k(\mathbf{X}_i) = \frac{1}{1 + (\theta_{ik}/f_d)^{f_e}} \quad (32)$$

where,  $y_k$  shows pixel membership value for cluster  $k$  and  $\theta_{ik}$  is GMM parameters for  $i^{th}$  data point and  $k^{th}$  cluster. The exponential factor ( $f_e$ ) and denominational fuzzy generators( $f_d$ ) are found empirically yields  $y_k$  in the interval of 0 and 1. The determined values of exponential factor and denominational fuzzy generators for brain MRI and ultrasound images are  $f_e = 5.5$  and  $5.3$ ,  $f_d = 1.1$ , respectively. The argmax function is used to obtain target cluster label.

### 3.2.2. Performance evaluation measures

The proposed approach has been evaluated on brain MRI and carotid artery ultrasound imaging modalities. Owing to the availability of ground truth images of MRI, following evaluation measures are utilized.

**3.2.2.1. Accuracy.** In classification, accuracy is the ratio of true predictions versus the total numbers of examined cases:

$$\text{Accuracy} = \frac{TP + TN}{P + N} \quad (33)$$

where,  $TP$ ,  $TN$ ,  $P$ , and  $N$  stands for true positive, true negative, total positive, and total negative samples, respectively.

**3.2.2.2. Jaccard similarity co-efficient (JSC).** Segmented image is analyzed quantitatively by using JSC index [41]. It is the ratio of intersection versus union of the output and actual segments. Closer the JSC value to 1 betters the segmentation quality. JSC index is computed by the following expression:

$$JSC(\text{Seg1}, \text{Seg2}) = \frac{|\text{Seg1} \cap \text{Seg2}|}{|\text{Seg1} \cup \text{Seg2}|} \quad (34)$$

**3.2.2.3. Dice similarity co-efficient (DSC).** DSC index is another parameter frequently used in the literature to evaluate image segmentation where ground truth is available [42]. DSC value close to 1 represents accurate segmentation.

$$DSC(\text{Seg1}, \text{Seg2}) = \frac{2|\text{Seg1} \cap \text{Seg2}|}{|\text{Seg1}| + |\text{Seg2}|} \quad (35)$$

**3.2.2.4. False positive ratio (FPR).** The FPR is ratio between false positive (FP) and the total predicted positive samples. Lower FPR value represents better classification performance [43]. To deal with multi-class problem, one versus all strategy is employed to compute FPR as under.

$$FPR = \frac{FP}{FP + TP} \quad (36)$$

**3.2.2.5. False negative ratio (FNR).** The FNR is ratio of false negative (FN) and total negative instances [44]. It ranges vary between 0 and 1 and computed by:

$$RFN = \frac{FN}{FN + TP} \quad (37)$$

**3.2.2.6. Segmentation performance evaluation for carotid artery ultrasound images.** Contrary to MRI, there is no ground truth available for evaluation of carotid artery segmentation. For this, we have used Davies Bouldin Index (DBI) [24] to validate the performance of the proposed approach.

$$DBI = \frac{1}{N} \sum_{i=1}^N D_i \quad (38)$$

$$D_i = \max_{i \neq j} R_{ij}$$

$$R_{ij} = \frac{S_i + S_j}{M_{ij}}$$

where, dispersion of  $i$  and  $j$  clusters is represented by  $S_i$ ,  $S_j$  and  $M_{ij}$  represents distance between the cluster centroids  $C_i$  and  $C_j$ .

The segmented ultrasound images are classified as normal or abnormal subject. For this purpose, SVM classifier is employed to IMT values measured from segmented images. The pseudo-code of the proposed approach is given in Fig. 2.

## 4. Results

Several experiments have been performed by employing the proposed approach based on Fig. 2 to segment brain MRI into four clusters: *white matter*, *background*, *cerebrospinal fluid*, and *gray matter*. The efficiency of the developed approach has been assessed using various performance evaluation measures. Additionally, it has been applied to a real problem of carotid artery plaque detection using ultrasound images. These images are segmented into three clusters: *arterial wall*, *carotid artery plaque*, and *background tissues*. The experimental results demonstrate that the proposed approach successfully detect plaque presented in carotid artery. Implementation is performed in MATLAB 9.4 (R2018a) using Intel i7 PC equipped with 12 GB of RAM.

In the following sub-sections, two case studies have been reported. Case-I depicts the segmentation results on brain MRI. In case-II, segmentation results of carotid artery ultrasound image are illustrated.

**Phase-I:****Feature Extraction**

- Step 1: MRI/Ultrasound image acquisition.
- Step 2: Extract the CWT, MGH and GLCM features with  $7 \times 7$  window size using Eqns. (1-11) and GLCM

**Parameter Initialization**

- Step 3: GMM Parameter Initialization

- Initialize cluster labels obtained by sFCM using Eqns. (12-16)
- GMM parameter estimation by using Eqns. (17-32)

**Model Evaluation**

- Step 4: Model Evaluation

- Performance measures for MRI using Eqns. (33-37)
- Performance evaluation for carotid artery ultrasound images (38)

**MRI Segmentation**

- Perform step 3 and evaluate the performance on the MRI test dataset
- Add various types of noise
- Assess the performance of the proposed technique utilizing ground truths to validate its robustness

**Phase-II:****Carotid Artery Ultrasound Images**

- Evaluate the performance on carotid artery images using parameters obtained from step 3
- Measure IMT values from segmented images
- Formulate a feature vector comprises of IMT values
- Perform SVM classification

**Compute classification evaluation measures**

- Accuracy, Sensitivity, Specificity, F-Score and MCC

**Fig. 2.** Pseudo-code of the proposed approach.**Table 1**

Quantitative performance of the proposed approach for segmented images of Fig. 3(b).

	Accuracy (%)	JSC	DSC	RFP	RFN
<b>Image1</b>	98.91	0.9783	0.9891	0.0058	0.0092
<b>Image2</b>	98.40	0.9685	0.9840	0.0099	0.0079
<b>Image3</b>	98.45	0.9695	0.9845	0.0073	0.0088
<b>Image4</b>	99.24	0.9849	0.9924	0.0086	0.0013

4.1. Case-I: performance results on brain MRI (Figs. 9, 10 and Tables 3–6)

4.1.1. Performance results on Gaussian noise

4.1.2. Performance results on Rician noise

4.2. Case-II: performance results on real carotid artery plaque detection (Figs. 11–14, Tables 7, 8)

## 5. Discussion

The experimental work has been carried out to evaluate the performance of the proposed approach employing on segmentation of brain MRI (case-I) and real carotid artery plaque ultrasound (case-II) images. For brain MRI segmentation evaluation, difference images have been obtained between the proposed approach segmentation and the ground truths as shown in Fig. 3. Visual analysis of the proposed segmentation in Fig. 3(b) is very close to the ground truth of the respective images. This analysis is validated from the difference image as shown in Fig. 3(c). Table 1 shows average of accuracy (98.69%), Jaccard similarity coefficient (97.53%), Dice similarity coefficient (98.75%), ratio of false positive (0.79%), and ratio of false negative (0.68%). These high values of different performance measures indicate the effectiveness of the proposed approach for segmentation of brain MRI.

Visual comparison among the proposed and several other techniques has been performed as shown in Fig. 4. From Table 2, the proposed approach achieved the maximum improvement in

**Table 2**

Quantitative performance of the proposed approach for segmented images of Fig. 4.

	Accuracy (%)	JSC	DSC	RFP	RFN
		Image 1			
FCM	98.3	0.968	0.981	0.112	0.011
K-MEANS	98.2	0.963	0.980	0.058	0.014
FRGMM [45]	82.8	0.706	0.828	0.171	0.172
<b>Proposed</b>	<b>98.4</b>	<b>0.978</b>	<b>0.988</b>	<b>0.019</b>	<b>0.013</b>
		Image 2			
FCM	98.8	0.984	0.988	0.010	0.018
K-MEANS	98.6	0.983	0.986	0.016	0.010
FRGMM [45]	85.3	0.744	0.853	0.138	0.147
<b>Proposed</b>	<b>99.1</b>	<b>0.982</b>	<b>0.991</b>	<b>0.008</b>	<b>0.001</b>
		Image 3			
FCM	98.0	0.968	0.980	0.019	0.012
K-MEANS	97.9	0.961	0.979	0.017	0.020
FRGMM [45]	84.8	0.736	0.848	0.152	0.183
<b>Proposed</b>	<b>98.2</b>	<b>0.969</b>	<b>0.982</b>	<b>0.016</b>	<b>0.010</b>

segmentation over FRGMM approach in term of JSC (23%). These visual and quantitative analysis indicate the usefulness of the proposed approach on the others.

To test the robustness of the proposed approach, it has been examined at various Gaussian noise levels. Gaussian noise is considered as common type of noise which has several reasons such as, electrons thermal vibrations and electronic circuit noise. In the experiments, Gaussian noise levels of 0.005, 0.007, 0.009, and 0.01 have been considered.

Fig. 5(a) shows the images corrupted with various Gaussian noise levels segmented by the proposed and other approaches. The visual inspection of Fig. 5 shows that the proposed technique offers superior segmentation as compared to the others. This robustness is majorly because of the incorporation of multiple image features and better GMM parameters estimation. These results demonstrate that the proposed technique prevails at even significant Gaussian image noise. By examining the objective measures in Table 3, it is evident that the proposed approach shows outstanding results at

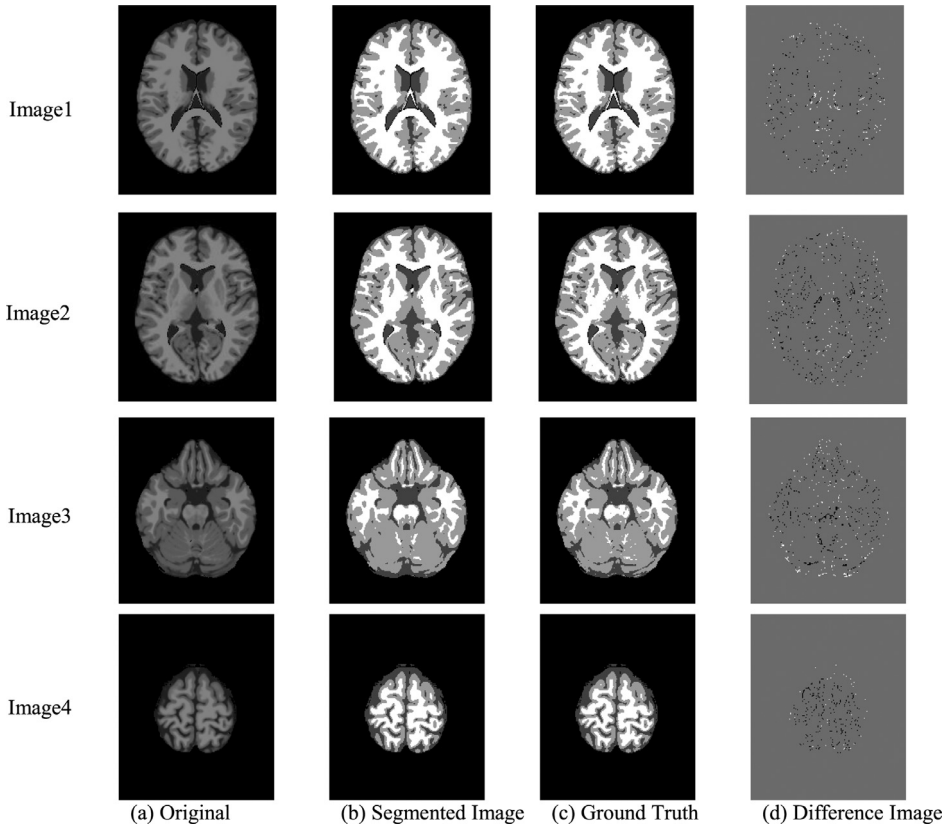


**Fig. 3.** The proposed approach segmentation along with ground truths and difference images.

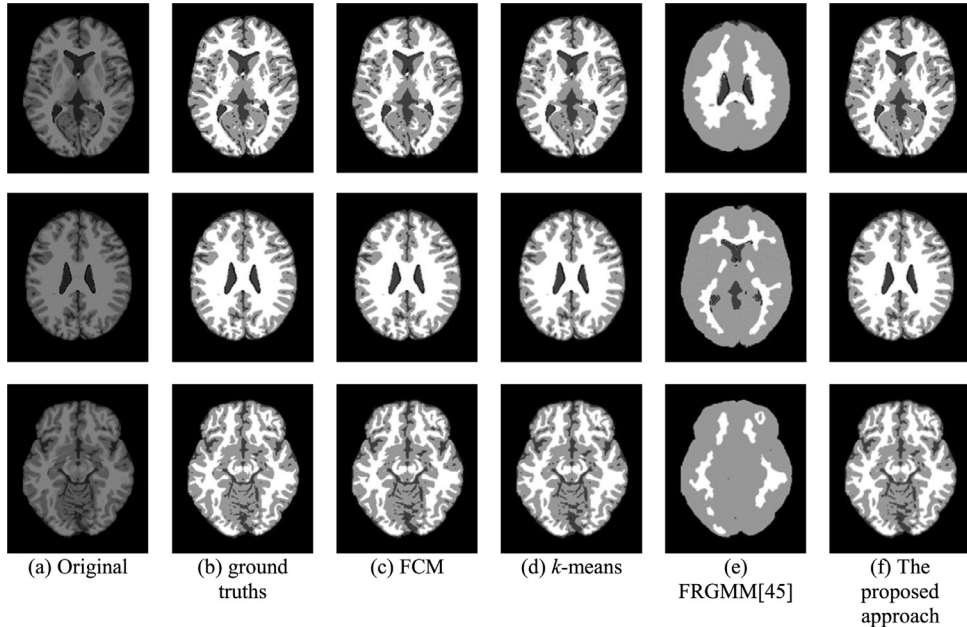


**Fig. 4.** Visual comparison of the proposed and various state-of-the art techniques.

the mentioned noise levels. It improves segmentation performance between 6.3–9.0% at various Gaussian noise levels.

The proposed technique has been applied to segment a sample brain MRI at the presence of various Rician noise levels of 3–9% as shown in Figs. 6, 7 and Tables 4, 5. These figures indicate that the proposed technique works well at increasing levels which is quantitatively validated as shown in Table 4 and 5. In similar fashion, the evaluation has been performed on Gaussian noise and

shown in Fig. 8 and Table 6 respectively. It is obvious from these results that our technique offers superior quality segmentation which shows its efficacy.

The illustrated results significantly improve segmentation performance at various noise types and levels. This outperformance is mainly because of the incorporation of sFCM for GMM parameters initialization. These GMM parameters have been approximated using maximum-likelihood with EM. Graphical comparison of the

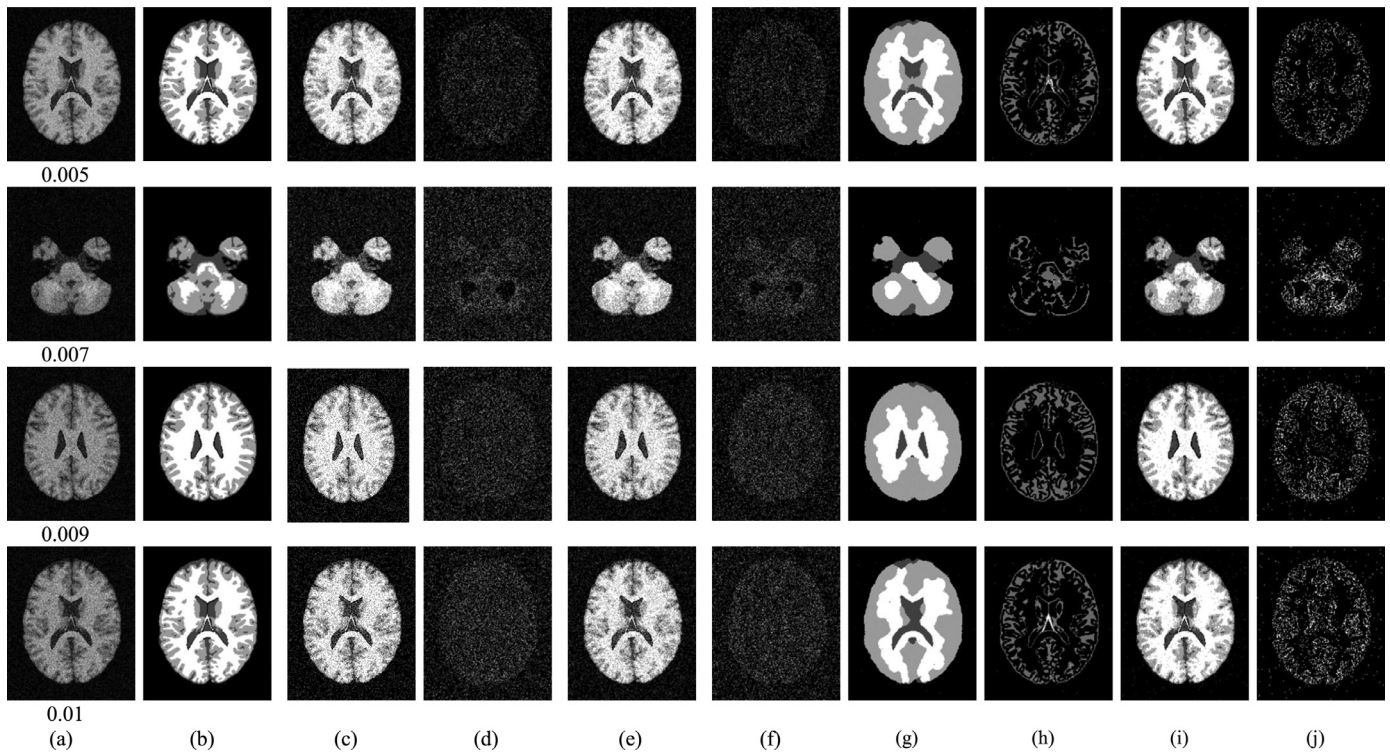


**Fig. 5.** (a) Bain MRI with Gaussian noise levels of 0.005, 0.007, 0.009, and 0.01, (b) ground truth images, (c) FCM clustering, (d) difference between the images (b) and (c), (e) K-means clustering, (f) difference between images (b) and (e), (g) FRGMM [45] clustering, (h) difference between the images (b) and (g), (i) proposed technique segmentation (j) difference between the images (b) and (i).

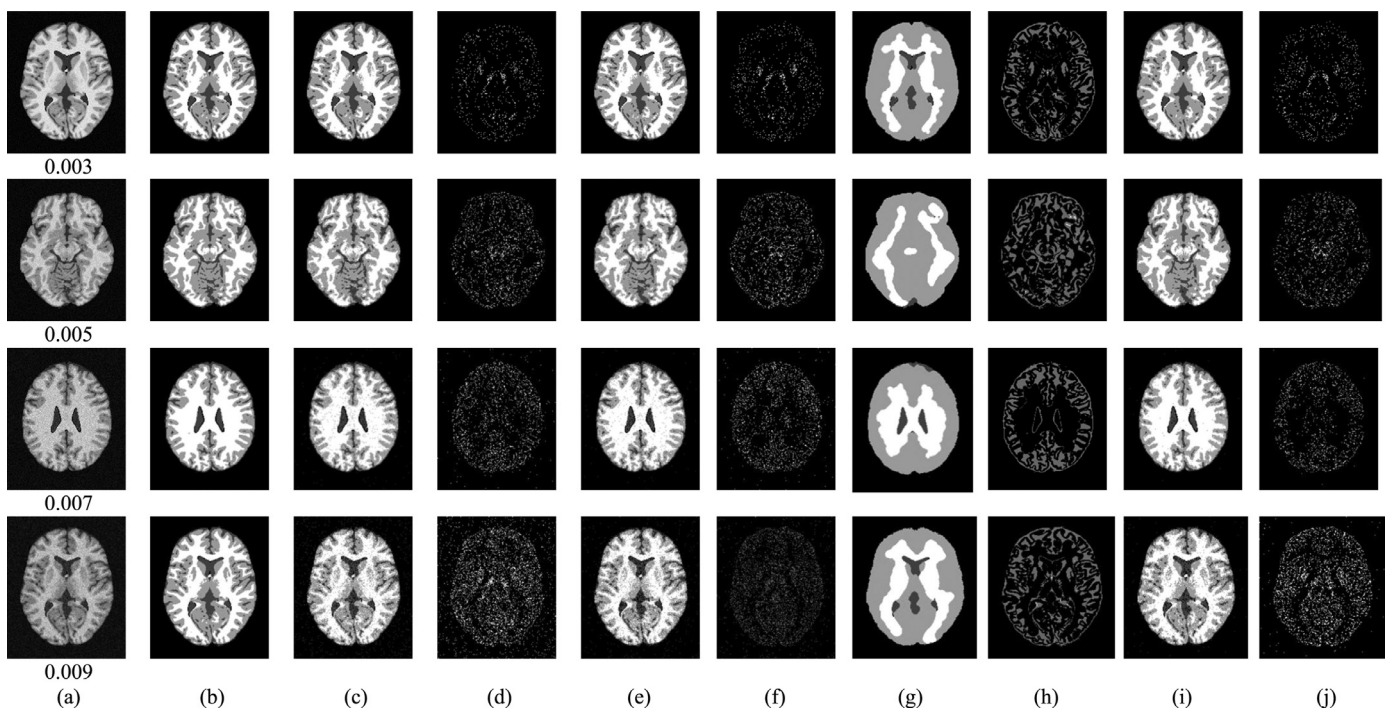


**Fig. 6.** (a) Brain MRI with Rician noise levels of 0.003, 0.005, 0.007 and 0.009, (b) ground truth image, (c) FCM clustering, (d) difference between the images (b) and (c), (e) K-means segmentation, (f) difference image between (b) and (e), (g) FRGMM [45] segmentation, (h) difference image between (b) and (g), (i) segmentation results of proposed algorithm (j) difference between the images (b) and (i).

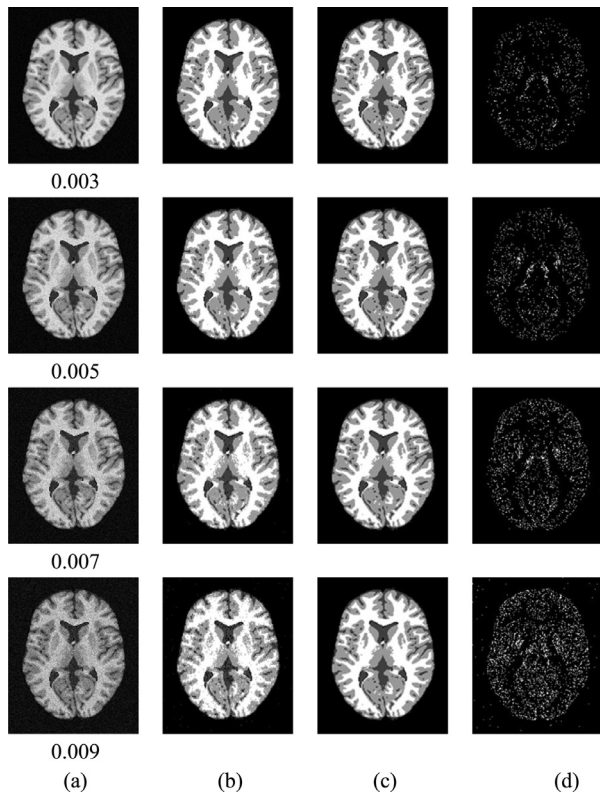


**Fig. 7.** (a) Brain MRI with Rician noise levels of 0.003, 0.005, 0.007, and 0.009, (b) Proposed segmentation, (c) Ground truth (d) Difference image between (c) and (b).

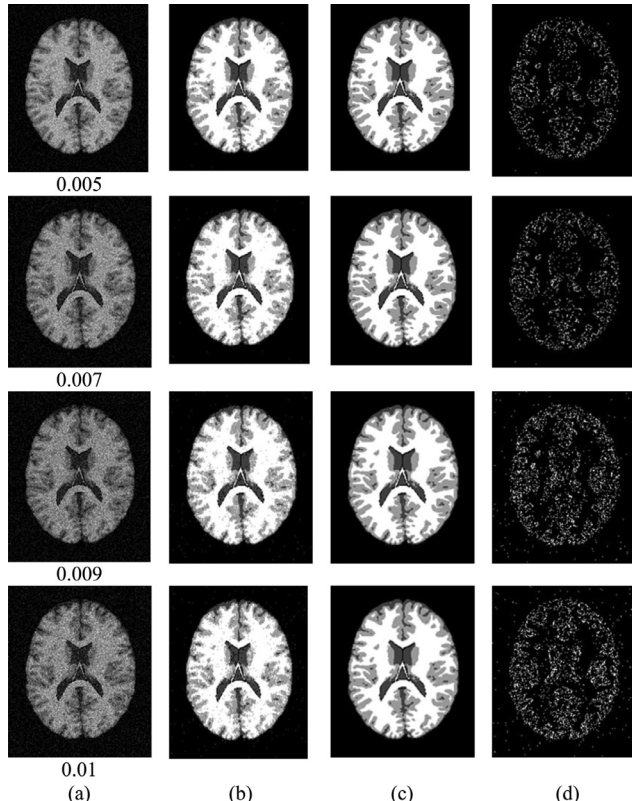


**Fig. 8.** (a) Brain MRI with Gaussian noise levels of 0.005, 0.007, 0.009, and 0.01 (b) proposed segmentation(c) ground truth image, (d) difference image between (c) and (b).

**Table 3**

Quantitative performance of the proposed approach at various Gaussian noise levels for segmented images of Fig. 5.

	Accuracy (%)	JSC	DSC	RFP	RFN
Gaussian noise level 0.005					
FCM	86.6	0.749	0.866	0.157	0.143
K-MEANS	86.4	0.761	0.864	0.135	0.205
FRGMM [45]	87.9	0.781	0.877	0.122	0.140
<b>Proposed</b>	<b>96.0</b>	<b>0.923</b>	<b>0.960</b>	<b>0.039</b>	<b>0.027</b>
Gaussian noise level 0.007					
FCM	74.5	0.593	0.745	0.285	0.260
K-MEANS	77.3	0.630	0.773	0.226	0.200
FRGMM [45]	94.0	0.889	0.941	0.058	0.038
<b>Proposed</b>	<b>95.9</b>	<b>0.922</b>	<b>0.959</b>	<b>0.040</b>	<b>0.029</b>
Gaussian noise level 0.009					
FCM	76.8	0.624	0.768	0.231	0.198
K-MEANS	77.9	0.638	0.779	0.220	0.199
FRGMM [45]	87.5	0.782	0.878	0.112	0.125
<b>Proposed</b>	<b>93.7</b>	<b>0.883</b>	<b>0.937</b>	<b>0.062</b>	<b>0.050</b>
Gaussian noise level 0.01					
FCM	75.7	0.609	0.757	0.221	0.242
K-MEANS	76.6	0.621	0.766	0.237	0.200
FRGMM [45]	87.5	0.778	0.875	0.124	0.162
<b>Proposed</b>	<b>93.1</b>	<b>0.872</b>	<b>0.931</b>	<b>0.063</b>	<b>0.051</b>

**Table 4**

Quantitative performance of the proposed approach at various Rician noise levels for segmented images of Fig. 6.

	Accuracy (%)	JSC	DSC	RFP	RFN
Rician noise level 0.003					
FCM	97.5	0.950	0.975	0.023	0.018
K-MEANS	97.6	0.951	0.976	0.022	0.017
FRGMM [45]	86.9	0.768	0.869	0.136	0.131
<b>Proposed</b>	<b>97.8</b>	<b>0.956</b>	<b>0.978</b>	<b>0.020</b>	<b>0.015</b>
Rician noise level 0.005					
FCM	96.2	0.928	0.962	0.037	0.037
K-MEANS	95.4	0.916	0.954	0.043	0.043
FRGMM [45]	85.0	0.850	0.740	0.149	0.149
<b>Proposed</b>	<b>96.5</b>	<b>0.932</b>	<b>0.965</b>	<b>0.031</b>	<b>0.034</b>
Rician noise level 0.007					
FCM	95.4	0.912	0.954	0.045	0.050
K-MEANS	95.4	0.913	0.954	0.045	0.050
FRGMM [45]	87.4	0.777	0.874	0.125	0.201
<b>Proposed</b>	<b>96.7</b>	<b>0.936</b>	<b>0.967</b>	<b>0.032</b>	<b>0.030</b>
Rician noise level 0.009					
FCM	90.3	0.822	0.902	0.102	0.010
K-MEANS	89.5	0.811	0.895	0.106	0.104
FRGMM [45]	85.1	0.740	0.851	0.148	0.151
<b>Proposed</b>	<b>92.6</b>	<b>0.963</b>	<b>0.926</b>	<b>0.078</b>	<b>0.069</b>

**Table 5**

Quantitative performance of the proposed approach at various Rician noise levels for segmented images of Fig. 7.

Noise levels	Accuracy (%)	JSC	DSC	RFP	RFN
<b>0.003</b>	97.6	0.954	0.976	0.023	0.020
<b>0.005</b>	96.6	0.935	0.966	0.030	0.028
<b>0.007</b>	95.0	0.905	0.950	0.049	0.039
<b>0.009</b>	92.6	0.863	0.925	0.073	0.060

**Table 6**

Quantitative performance of the proposed approach at various Gaussian noise levels for segmented images of Fig. 8.

Noise levels	Accuracy (%)	JSC	DSC	RFP	RFN
<b>0.005</b>	96.0	0.923	0.960	0.038	0.030
<b>0.007</b>	94.9	0.904	0.949	0.050	0.042
<b>0.009</b>	93.5	0.879	0.935	0.064	0.060
<b>0.01</b>	93.1	0.872	0.931	0.068	0.065

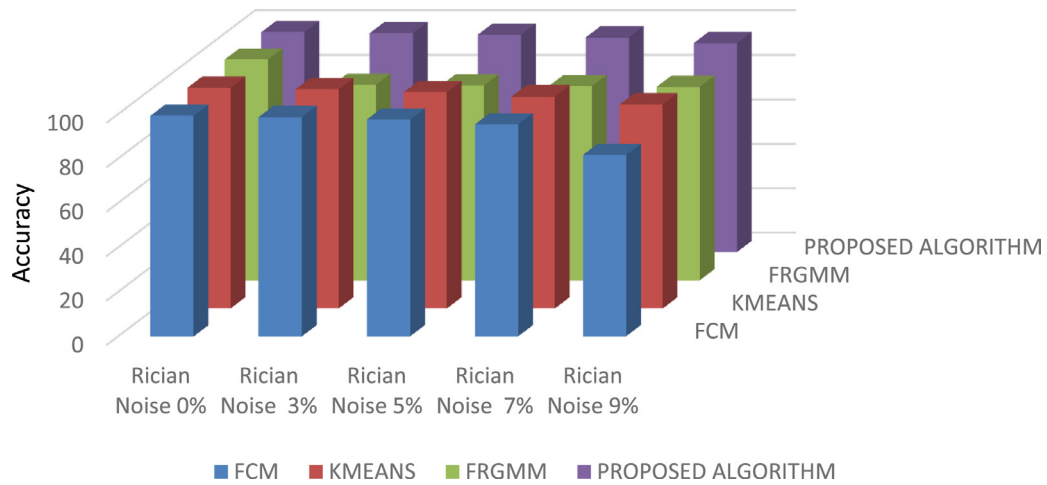


**Fig. 9.** Average performance comparison of the proposed and other approaches at various Rician noise levels.

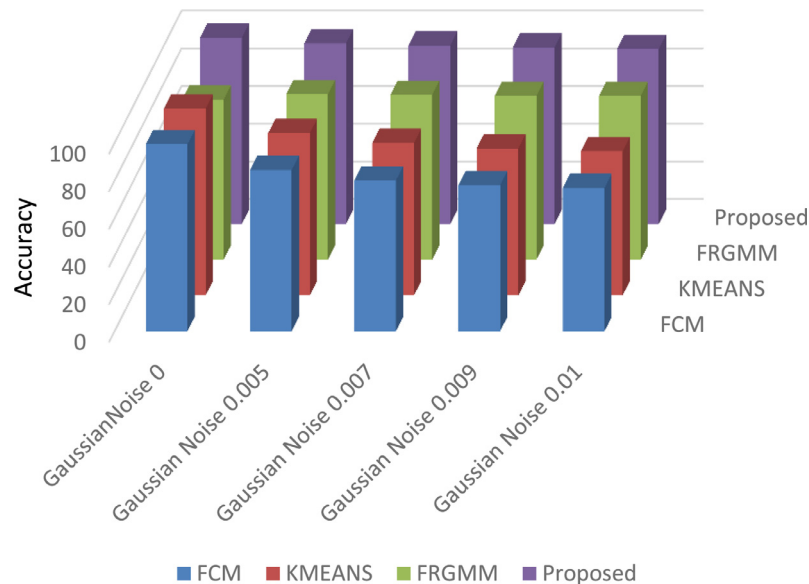


**Fig. 10.** Average performance comparison of the proposed and other approaches at various Gaussian noise levels.

proposed and other techniques on Rician and Gaussian noise levels is shown in Figs. 9 and 10, respectively.

Keeping in view the superior segmentation performance of the proposed approach on brain MRI, this inspired us to develop an application for carotid artery plaque detection. The classification of plaque critically depends upon accurate segmentation. For this, firstly carotid artery walls have been separated from background tissues in the ultrasound images. Then, IMT values have been measured from segmentation followed by SVM classification. In this application, all segmentation steps have been performed similar to case-I, except the input image. Fig. 11, shows a real carotid artery ultrasound image in which artery plaque is marked by the radiologist highlighted within a rectangular box. The magnified version of ROI is shown in Fig. 12(a) which has been segmented by the proposed approach as shown in Fig. 12(b).

It is evident from Fig. 12(b) that our approach successfully separates arterial walls from the background tissues. Here, some mislabeled spots have been observed in the segmented image which is because of low quality of ultrasound images. To minimize these spots, morphological correction (erosion followed dilation) has been employed to the segmented image as given in Fig. 12(c). For visual assessment, the proposed approach segmented image

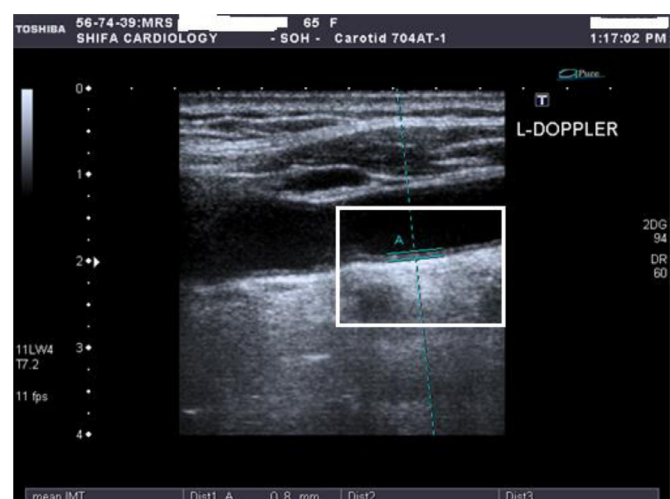


**Fig. 11.** A real carotid artery ultrasound image with marked ROI (name of patient has been erased for privacy).

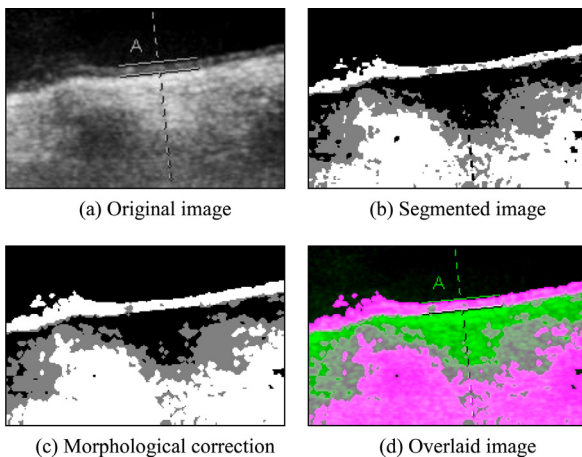


**Fig. 12.** Stepwise output images by the proposed approach.

is overlaid on the original as shown in Fig. 12(d) which is used for IMT measurements. Similarly, the whole carotid artery dataset is segmented and IMT values are measured hence used for classification. For visualization, some sample carotid artery images segmented by our approach are shown in Fig. 13. It is apparent from the segmentation results that the proposed approach successfully separates ROI from background tissues. Additionally for quantitative assessment, Davies Bouldin index (DBI) of each segmented image and shown in Table 7. The lower value of DBI indicates better segmentation.

The post-processing step (in our case is classification) which majorly depends upon quality segmentation. The proposed approach successfully addresses the challenging problem of plaque

**Table 7**  
Quantitative performance of the proposed approach for segmented images of Fig. 13.

Fig. 13	DBI value
Image-1	0.4013
Image-2	0.3962
Image-3	0.4150
Image-4	0.4210

separation, hence used to classify into normal or abnormal subject. The mean and standard deviation of IMT values of normal and abnormal arterial walls are 0.392 mm, 0.109 mm, 0.775 mm, and 0.173 mm, respectively as shown in Fig. 14. The statistical features of average, standard deviation, variance, skewness, maximum, and minimum of IMT values are computed for each subject [11] and feed to SVM classifier. The plaque detection performance using SVM is shown in Table 8. This table shows that SVM outperforms and offers a high classification accuracy of 98.8% which shows its usefulness. Furthermore, other classification evaluation parameters has been computed and shown in Table 8. The performance analysis of the proposed approach indicates that it is feasible for carotid artery plaque detection. The proposed technique results are compared with some already published techniques. For instance, Santhiyakumari et al. [46] and Hassan et al. [11] both uses multilayer back-propagation neural networks (MLBPNN) and reported accuracy of 96% and 98.4% respectively. Whereas, we have achieved a high classification accuracy of 98.8%.

The proposed technique outperforms, owing to the efficient use of GMM, sFCM and relevant features extraction techniques which followed by SVM classification. It has several advantages over conventional segmentation techniques, for instance; (i) the

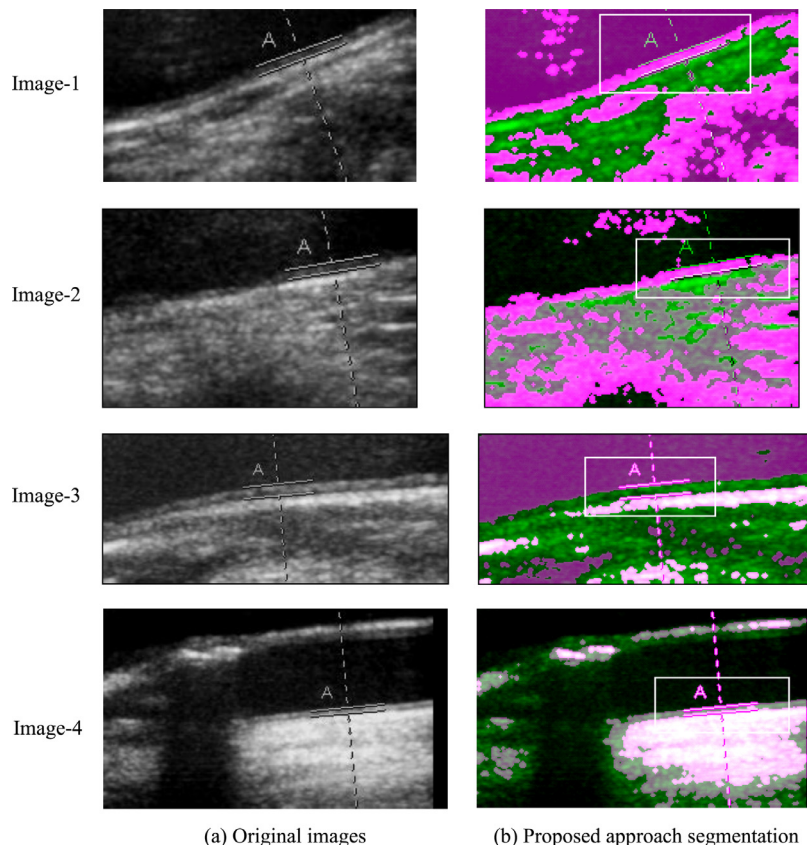


**Fig. 13.** Original and segmented real carotid artery ultrasound images.

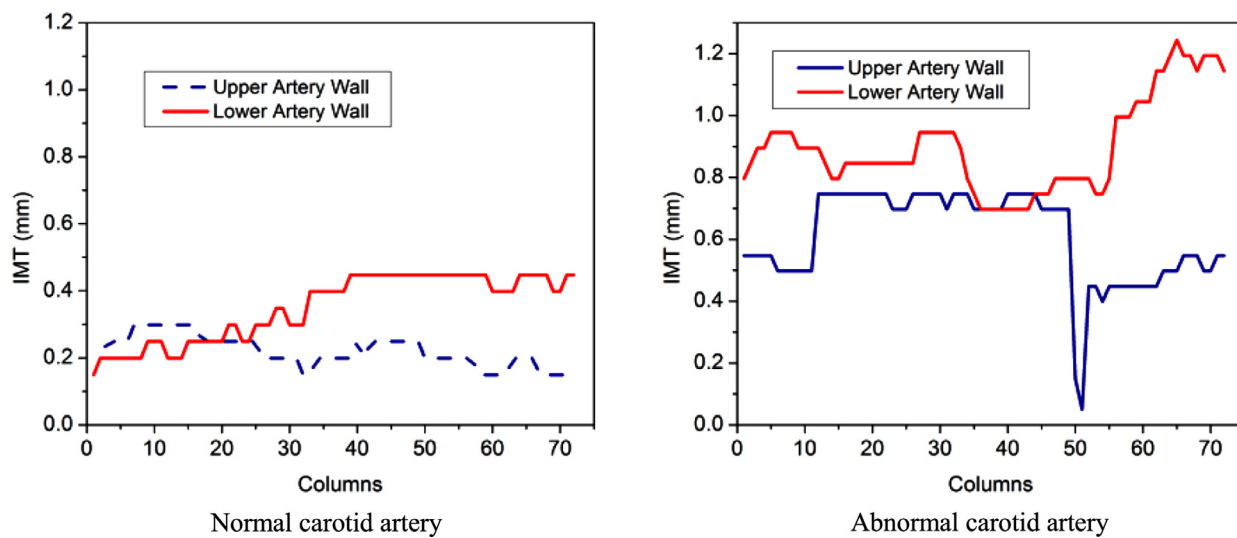


Fig. 14. IMT values of a normal and abnormal carotid artery.

**Table 8**  
Classification performance comparison of the proposed SVM based approach and others.

Approach	Accuracy (%)	Sensitivity	Specificity	F-score	MCC
<b>Proposed</b>	98.80	0.993	0.98	0.990	0.975
Hassan et al. [11]	98.40	0.99	0.93	0.963	0.925
Santhiyakumari et al. [46]	96.00	0.90	0.95	–	–

proposed technique address the problem of noise in brain MRI and improved segmentation significantly in both Gaussian and Rician noises. (ii) The proposed technique also solved a challenging real world problem of carotid artery plaque detection using low quality ultrasound images. Early detection of plaque in carotid artery may prevent from serious brain strokes. (iii) The proposed technique might be deployed to clinic and can easily be used by the practitioners. On the other hand, the proposed technique has limitation in model formation and training. The training process involves sufficient data along with accurate identification of region of interest (ROI). Once, it is done the proposed technique can successfully utilized for the other imaging modalities. Further, effectiveness of this technique is validated by the experimental results for both medical image modalities (MRI and Ultrasound).

In medical domain, there is a tradeoff between diagnosis accuracy versus computational cost. In this research, we give due consideration to improve diagnosis accuracy of the developed models at the expense of some additional steps. These steps involve GMM parameters estimation that does not involve any memory intensive data structures.

The proposed study has clinical significance as it provides safe and noninvasive imaging tool for quick and effective screening during routine cardiology referrals. It may help to improve the clinical evaluation of this disease in both asymptomatic and symptomatic patients. It is practical to deploy this technique to clinic and can easily be used by the practitioner as automated screening tool.

## 6. Conclusions

In this research, a novel segmentation approach for MRI and ultrasound imaging modalities is proposed. Owing to the inherent degradations in MRI and ultrasound images, segmentation

challenges were addressed. Experiments have been performed on both modalities in which the proposed approach demonstrates outstanding performance. The proposed technique offers high segmentation accuracy of 99% on brain MRI which improved segmentation results by 3–9% as compared to the well-known segmentation techniques. The proposed approach outperformed due to (i) effective use of GMM, sFCM and relevant image descriptors extraction, (ii) EM algorithm automatically updates GMM parameters, (iii) EM algorithm effectively estimate the latent variables in the presence of noise, and (iv) GMM parameters estimation does not involve any memory intensive data structures. Moreover, the developed approach is applied to carotid artery plaque diagnosis. The dataset of real carotid artery ultrasound images were obtained from Shifa International Hospital Islamabad, Pakistan. Plaque detection was achieved using SVM classifier which offers a high accuracy of 98.8%. The developed approach is straightforward, effective, and reproducible. It may benefit to improve the clinical evaluation of this disease in both asymptomatic and symptomatic individuals. It is practical to deploy this technique to clinics and can easily be used by the practitioner as automated screening tool. Owing the capability of successful segmentation of MRI and ultrasound images, it may be extended for other medical image modalities for disease diagnosis.

## Conflict of Interest

This research has not received any grant from any funding organizations. The authors declare that they have no conflict of interest.

## Acknowledgment

We are thankful to Radiology Department, Shifa International Hospital Islamabad, Pakistan for providing data and its annotations.

## References

- [1] Z. Yang, F.-L. Chung, W. Shitong, Robust fuzzy clustering-based image segmentation, *Appl. Soft Comput.* 9 (2009) 80–84.
- [2] D. Velakoulis, S.J. Wood, M.T. Wong, P.D. McGorry, A. Yung, L. Phillips, D. Smith, W. Brewer, T. Proffitt, P. Desmond, Hippocampal and amygdala volumes according to psychosis stage and diagnosis: a magnetic resonance imaging study of chronic schizophrenia, first-episode psychosis, and ultra-high-risk individuals, *Arch. Gen. Psychiatry* 63 (2006) 139–149.
- [3] J. Tan, D.L. Joon, G. Fitt, M. Wada, M.L. Joon, A. Mercuri, M. Marr, M. Chao, V. Khoo, The utility of multimodality imaging with CT and MRI in defining rectal tumour volumes for radiotherapy treatment planning: a pilot study, *J Med. Imaging Radiat. Oncol.* 54 (2010) 562–568.
- [4] S.M. Smith, P.T. Fox, K.L. Miller, D.C. Glahn, P.M. Fox, C.E. Mackay, N. Filippini, K.E. Watkins, R. Toro, A.R. Laird, Correspondence of the brain's functional architecture during activation and rest, *Proc Natl. Acad. Sci.* 106 (2009) 13040–13045.
- [5] A. Chaudhry, M. Hassan, A. Khan, J.Y. Kim, T.A. Tuan, Image clustering using improved spatial fuzzy C-means, in: Proceedings of the 6th International Conference on Ubiquitous Information Management and Communication, ACM, 2012, p. 86.
- [6] M. Tahir, B. Jan, M. Hayat, S.U. Shah, M. Amin, Efficient computational model for classification of protein localization images using Extended Threshold Adjacency Statistics and support vector machines, *Comput. Methods Programs Biomed.* 157 (2018) 205–215.
- [7] J.L. Garcia-Arroyo, B. Garcia-Zapirain, Segmentation of skin lesions in dermoscopy images using fuzzy classification of pixels and histogram thresholding, *Comput. Methods Programs Biomed.* 168 (2019) 11–19.
- [8] N. Ayache, Segmentation of complex three-dimensional medical objects: a challenge and a requirement for computer-assisted surgery planning and performance, 96, Taylor, 1996.
- [9] A.E. Hassaniene, H.M. Moftah, A.T. Azar, M. Shoman, MRI breast cancer diagnosis hybrid approach using adaptive ant-based segmentation and multilayer perceptron neural networks classifier, *Appl. Soft Comput.* 14 (2014) 62–71.
- [10] S.L. Murphy, J. Xu, K.D. Kochanek, National Vital Statistics Report, National Center for Health Statistics, Hyattsville, 2013.
- [11] M. Hassan, A. Chaudhry, A. Khan, J.Y. Kim, Carotid artery image segmentation using modified spatial fuzzy c-means and ensemble clustering, *Comput. Methods Programs Biomed.* 108 (2012) 1261–1276.
- [12] R.-M. Menchón-Lara, M.-C. Bastida-Jumilla, J. Morales-Sánchez, J.-L. Sancho-Gómez, Automatic detection of the intima-media thickness in ultrasound images of the common carotid artery using neural networks, *Med. Biol. Eng. Comput.* 52 (2014) 169–181.
- [13] F. Bozkurt, C. Köse, A. Sarı, An inverse approach for automatic segmentation of carotid and vertebral arteries in CTA, *Expert Syst. Appl.* 93 (2018) 358–375.
- [14] S. Moccia, E. De Momi, S. El Hadji, L.S. Mattos, Blood vessel segmentation algorithms – review of methods, datasets and evaluation metrics, *Comput. Methods Programs Biomed.* 158 (2018) 71–91.
- [15] D.L. Pham, Spatial models for fuzzy clustering, *Comput. Vision Image Understanding* 84 (2001) 285–297.
- [16] T.K. Moon, The expectation-maximization algorithm, signal processing magazine, IEEE 13 (1996) 47–60.
- [17] T.M. Nguyen, Q. Wu, Fast and robust spatially constrained gGaussian mixture model for image segmentation, *IEEE Trans., Circuits Syst. Video Technol.* 23 (2013) 621–635.
- [18] A. Mayer, H. Greenspan, An adaptive mean-shift framework for MRI brain segmentation, *Med. Imaging, IEEE Trans.* 28 (2009) 1238–1250.
- [19] Z. Wang, Q. Song, Y.C. Soh, K. Sim, An adaptive spatial information-theoretic fuzzy clustering algorithm for image segmentation, *Comput. Vision Image Understanding* 117 (2013) 1412–1420.
- [20] Z. Iscan, A. Yüksel, Z. Dokur, M. Korürek, T. Ölmez, Medical image segmentation with transform and moment based features and incremental supervised neural network, *Digit. Signal Process.* 19 (2009) 890–901.
- [21] A. Benachouche, H. Oulhadj, P. Siarry, Improved spatial fuzzy c-means clustering for image segmentation using PSO initialization, Mahalanobis distance and post-segmentation correction, *Digit. Signal Process.* 23 (2013) 1390–1400.
- [22] Z. Ji, Y. Xia, Q. Chen, Q. Sun, D. Xia, D.D. Feng, Fuzzy c-means clustering with weighted image patch for image segmentation, *Appl. Soft Comput.* 12 (2012) 1659–1667.
- [23] Z. Ji, J. Liu, G. Cao, Q. Sun, Q. Chen, Robust spatially constrained fuzzy c-means algorithm for brain MR image segmentation, *Pattern Recognit.* 47 (2014) 2454–2466.
- [24] A. Chaudhry, M. Hassan, A. Khan, Robust segmentation and intelligent decision system for cerebrovascular disease, *Med. Biol. Eng. Comput.* 54 (2016) 1903–1920.
- [25] M. Yousuf, M. Nobi, A new method to remove noise in magnetic resonance and ultrasound images, *J. Sci. Res.* 3 (2011) 81.
- [26] K.-S. Chuang, H.-L. Tzeng, S. Chen, J. Wu, T.-J. Chen, Fuzzy c-means clustering with spatial information for image segmentation, *Comput. Med. Imaging Graph.* 30 (2006) 9–15.
- [27] A. Chaudhry, M. Hassan, A. Khan, J.Y. Kim, T.A. Tuan, Image clustering using improved spatial fuzzy C-means, in: Proceedings of the 6th International Conference on Ubiquitous Information Management and Communication, ACM, Kuala Lumpur, Malaysia, 2012.
- [28] B.N. Li, C.K. Chui, S. Chang, S.H. Ong, Integrating spatial fuzzy clustering with level set methods for automated medical image segmentation, *Comput. Biol. Med.* 41 (2011) 1–10.
- [29] M. Hassan, A. Chaudhry, A. Khan, Carotid artery image segmentation using modified spatial fuzzy c-means and ensemble clustering, *Comput. Methods Programs Biomed.* 108 (2012) 1261–1276, doi:10.1016/j.cmpb.2012.1008.1011.
- [30] C.A. Cocosco, V. Kollokian, R.K.-S. Kwan, G.B. Pike, A.C. Evans, Brainweb: online interface to a 3D MRI simulated brain database, *NeuroImage*, Citeseer (1997).
- [31] M. Tahir, A. Khan, A. Majid, Protein subcellular localization of fluorescence imagery using spatial and transform domain features, *Bioinformatics* 28 (2011) 91–97.
- [32] H. Sheshadri, A. Kandaswamy, Experimental investigation on breast tissue classification based on statistical feature extraction of mammograms, *Comput. Med. Imaging Graph.* 31 (2007) 46–48.
- [33] R. Polikar, Fundamental concepts & an overview of the wavelet theory. Tutorial, 1996.
- [34] J. Ma, Z. Wang, M. Vo, L. Luu, Parameter discretization in two-dimensional continuous wavelet transform for fast fringe pattern analysis, *Appl. Opt.* 50 (2011) 6399–6408.
- [35] M. Tahir, Pattern analysis of protein images from fluorescence microscopy using Gray Level Co-occurrence Matrix, *J. King Saud Univ. - Sci.* 30 (2018) 29–40.
- [36] C.B. James, *Pattern Recognition With Fuzzy Objective Function Algorithms*, Kluwer Academic Publishers, 1981.
- [37] K.-S. Chuang, H.-L. Tzeng, S. Chen, J. Wu, T.-J. Chen, Fuzzy c-means clustering with spatial information for image segmentation, *Comput. Med. Imaging Graph.* 30 (2006) 9–15.
- [38] H. Greenspan, A. Ruf, J. Goldberger, Constrained Gaussian mixture model framework for automatic segmentation of MR brain images, *Med. Imaging, IEEE Trans.* 25 (2006) 1233–1245.
- [39] S. Borman, The expectation maximization algorithm-a short tutorial, Submitted for publication, (2004) 1–9.
- [40] S. Mitra, J. Basak, FRBF: A Fuzzy Radial Basis Function Network, *Neural Comput. Appl.* 10 (2001) 244–252.
- [41] U. Vovk, F. Pernus, B. Likar, A review of methods for correction of intensity inhomogeneity in MRI, *IEEE Trans. Med. Imaging* 26 (2007) 405–421.
- [42] K.H. Zou, S.K. Warfield, A. Bharatha, C.M. Tempany, M.R. Kaus, S.J. Haker, W.M. Wells III, F.A. Jolesz, R. Kikinis, Statistical validation of image segmentation quality based on a spatial overlap index1: scientific reports, *Acad. Radiol.* 11 (2004) 178–189.
- [43] R.-L. Hsu, M. Abdel-Mottaleb, A.K. Jain, Face detection in color images, *IEEE Trans Pattern Anal. Mach. Intell.* 24 (2002) 696–706.
- [44] K. Veropoulos, C. Campbell, N. Cristianini, Controlling the sensitivity of support vector machines, in: Proceedings of the international joint conference on AI, 1999, p. 60.
- [45] T.M. Nguyen, Q.M.J. Wu, Fast and robust spatially constrained Gaussian Mixture Model for image segmentation, *IEEE Trans. Circuits Syst. Video Technol.* 23 (2013) 621–635.
- [46] N. Santhiyakumari, P. Rajendran, M. Madheswaran, Medical decision-making system of ultrasound carotid artery intima–media thickness using neural networks, *J Digit. Imaging* 24 (2011) 1112–1125.